Water Research 303 (2026) 126201

Contents lists available at ScienceDirect

Water Research

journal homepage: www.elsevier.com/locate/watres

A PFAS-selective semifluoroalkylated polyvinylimidazolium resin for reversible adsorption of anionic fluorosurfactants

Judith Schobel [a,b,1], Johanna Freilinger [b,1], Jana Marx [a,c], Madeleine Larch [a], Martin Spruck [a], Raphael Plangger [d], Marco Rupprich [e], Herwig Schottenberger [f], Christian W. Huck [b], Rania Bakry [b,2], Jan O. Back [a,*]

[a] Department of Environmental, Process & Energy Engineering, MCI – The Entrepreneurial School, Innsbruck, Austria
[b] Institute of Analytical Chemistry and Radiochemistry, Leopold-Franzens University Innsbruck, Austria
[c] Research Institute of Textile Chemistry and Textile Physics, Leopold-Franzens University Innsbruck, Austria
[d] Institute of Organic Chemistry and Center for Molecular Biosciences Innsbruck (CMBI), Leopold-Franzens University Innsbruck, Austria
[e] Institute for Ecopreneurship, School of Life Sciences, University of Applied Sciences and Arts Northwestern Switzerland (FHNW), Muttenz, Switzerland
[f] Institute of General, Inorganic and Theoretical Chemistry, Leopold-Franzens University Innsbruck, Austria

HIGHLIGHTS

- FP-AER: co-localized imidazolium and perfluoroalkyl moieties within robust backbone.
- Dual-mode sorption mechanism with synergistic electrostatic and F···F interactions.
- High PFAA capacities at low c_{eq}, surpassing literature benchmarks.
- Fixed-bed column tests confirm scalability and short/long-chain species removal.
- Efficient regeneration using methanol–salt eluents with >90 % recovery.

GRAPHICAL ABSTRACT

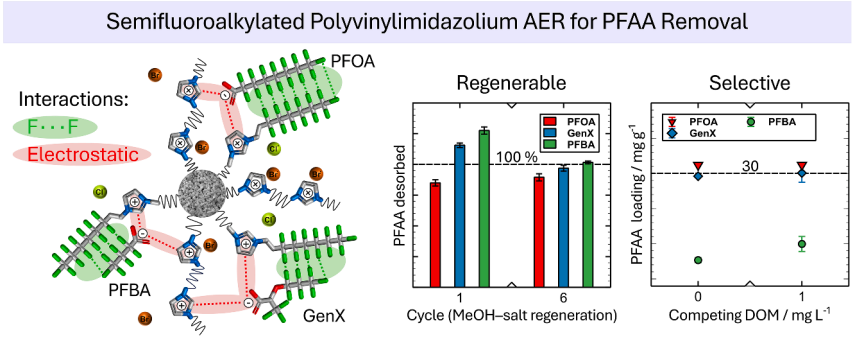

ARTICLE INFO

Keywords:
PFAS adsorption
Fluorinated polymer
Anion exchange resin
Dual-mode binding mechanism
Regeneration

ABSTRACT

Per- and polyfluoroalkyl substances (PFAS) in drinking-water sources demand sorbents that capture both long- and short-chain species and can be efficiently regenerated. A hydrolytically robust fluorinated polymer is reported, in which cationic heteroaromatic charges and perfluoroalkyl moieties are co-localized within each operative functionality. Thus, dual-mode binding sites matching electrostatic and fluorophilic attraction were evaluated as sorbent design for anionic fluorosurfactants. The fluorinated polymer-based anion exchange resin (FP-AER) was synthesized via UV-initiated copolymerization of a perfluoroalkyl-tethered vinylimidazolium monomer with a bis-vinylimidazolium crosslinker and comprehensively characterized by physicochemical methods. Batch adsorption assays versus powdered activated carbon (PAC) quantified single- and multicomponent isotherms, kinetics, co-solute and ionic-strength effects, regeneration, and performance in spiked aqueous

* Corresponding author.
E-mail address: jan.back@mci.edu (J.O. Back).
[1] These authors contributed equally to this work.
[2] Author passed away before publication of this work.

https://doi.org/10.1016/j.watres.2026.126201
Received 2 March 2026; Received in revised form 25 May 2026; Accepted 26 May 2026
Available online 2 June 2026

film-forming foam (AFFF)-impacted groundwater. FP-AER achieved Langmuir capacities of 597 mg g^{-1} (PFOA) and 143 mg g^{-1} (GenX); PFBA exhibited near-linear Freundlich behaviour. At a benchmark equilibrium concentration of 50 μg L^{-1}, FP-AER outperformed PAC by 3–9-fold. The adsorbent was selective in the presence of organic micropollutants (OMPs) and showed pronounced sensitivity to chloride. Regeneration using methanol–salt eluents yielded >90 % recoveries across at least six cycles. In AFFF-impacted groundwater spiked at 0.5 μg L^{-1} per PFAS, batch tests confirm high PFAS removal by FP-AER relative to PAC. Exploratory rapid small-scale column tests (RSSCTs) demonstrated feasibility under continuous-flow conditions. A focused mini-review and comparative benchmarking contextualize FP-AER against established AERs and emerging fluorinated sorbents, highlighting the remarkable capacity of the developed dual-mode sorbent; future work will target lower influent levels and optimized column operation.

1. Introduction

Per- and polyfluoroalkyl substances (PFAS) are persistent, mobile, and increasingly regulated due to toxicological concerns and widespread occurrence in drinking-water sources (Glüge et al., 2020). In response to restrictions on long-chain PFAS, particularly PFAS-acids (PFAAs), industry has shifted towards short-chain analogues (< C7) to reduce bioaccumulation hazards (Li et al., 2020). However, short-chain PFAS are more mobile, less amenable to adsorption, and can pose similar health risks (Gagliano et al., 2020; Zhang et al., 2019). Drinking water is a major exposure pathway (Crone et al., 2019), and regulatory limits continue to become increasingly stringent (Cousins et al., 2022; Dong et al., 2025), for instance, 100 ng L^{-1} for PFAS-20 in the EU (introduced in 2020; European Parliament, 2020), and for PFAS-4, limits have recently been reduced to 20, 4, and 2 ng L^{-1} in Germany (Federal Republic of Germany (Bundesrepublik Deutschland), 2023), Sweden (Swedish Food Agency (Livsmedelsverket), 2023), and Denmark (Danish Ministry of Environment and Gender Equality (Miljøministeriet), 2021), respectively, in consideration of an opinion by the European Food Safety Authority (EFSA) released in 2020 (Schrenk et al., 2020); England and Wales specify 100 ng L^{-1} for 48 selected PFAS (Drinking Water Inspectorate, 2025).

Among treatment options, dense-membrane processes (e.g., reverse osmosis, RO) can achieve high removal but entail high energy use and retentate management (Das and Ronen, 2022). Consequently, adsorption remains the most widely deployed approach, particularly by means of powdered/granular activated carbon (AC) and anion-exchange resins (AER) (Zhang et al., 2019). AC relies primarily on hydrophobic interactions and performs well for long-chain PFAS, but is less effective for short-chain species (Gagliano et al., 2020). AERs rely on electrostatic interactions between anionic PFAA headgroups and cationic sites; they offer faster kinetics and smaller footprints (Dixit et al., 2021), yet performance is sensitive to ionic strength, pH, natural organic matter (NOM), and co-contaminants (Boyer et al., 2021).

To improve selectivity, recent work has explored fluorinated sorbents that leverage fluorophilicity – favourable interactions among perfluoroalkyl fragments (F···F interactions) arising from strong C–F bond polarity coupled with low polarizability and distinctive dispersion forces (Fu et al., 2024; He et al., 2024). Therefore, perfluoroalkyl chains also tend to self-associate and partition into “fluorous” phases that are both lipophobic and hydrophobic, providing a driving force for PFAS tails to leave the aqueous phase and reside in fluorinated microenvironments (Fu et al., 2024). Importantly, this fluorophilic behaviour is distinct from generic hydrophobicity: while fluorosurfactants possess polar headgroups with affinity for water, their perfluoroalkyl tails are broadly omniphobic – repelling both aqueous environments and conventional organic frameworks (e.g., polyacrylic or polystyrenic hydrocarbon backbones of common AERs). As a result, fluorous functionalities offer preferential microenvironments for PFAS tails that are not readily mimicked by non-fluorous hydrophobic matrices.

While such fluorinated segments enhance selectivity, established fluorosorbents bearing only a single binding-responsive functionality often show limited PFAA capacities at low concentrations (Koda et al., 2015; Tan et al., 2021, 2022b). This motivates genuine dual-mode affinity designs that combine fluorinated domains with cationic sites to establish cooperative molecular architectures, i.e. combining F···F interactions (tails) with coulombic attraction (anionic headgroups).

Here, we showcase a hydrolytically robust, semifluoroalkylated polymer, hereafter FP-AER, prepared from 3-(1*H*,1*H*,2*H*,2*H*-perfluorooctyl)-1-vinylimidazolium chloride, a commercially available monomer (Partl et al., 2021). Unlike AER materials that rely on separated charged constituents and remote perfluoroalkyl tails (Chavan et al., 2018; Román Santiago et al., 2023), our design leverages a fluorinated cationic imidazolium monomer paired with a crosslinker – also permanently cationic – to copolymerize via free-radical polymerization and co-localize the strong-base site and perfluoroalkyl domain within each repeat unit, with charged site density and F content controlled by monomer–crosslinker stoichiometry. Sorption thus proceeds via two synergistic interactions at a single binding site: ion-exchange of anionic headgroups at the imidazolium and fluorophilic interactions of tails with the attached fluoroponytail. By using a durable polyethylene backbone, leaching risks are minimized relative to siloxane- or ester-containing supports (Kumarasamy et al., 2020; Singh et al., 2023).

The study presents the synthesis and thorough physicochemical characterization of FP-AER, followed by systematic adsorption assays (single- and multicomponent isotherms and kinetics), co-solute and ionic-strength effects, and regeneration testing. Performance is also examined in an AFFF-impacted groundwater matrix. We also include a focused mini-review and benchmarking to position FP-AER among conventional AERs and emerging fluorinated sorbents.

2. Materials and methods

2.1. Materials

The following chemicals were used: acetonitrile (ACN), ammonium acetate, ammonium chloride, 2,2-dimethoxy-2-phenylacetophenone (DMPA), formic acid (FA), methanol (MeOH), lithium chloride, 1-propanol, sodium bicarbonate, sodium carbonate, sodium chloride, and sodium iodide.

The PFAS used were: perfluorobutanoic acid (PFBA), nonafluorobutane-1-sulfonic acid (PFBS), perfluoropentanoic acid (PFPeA), ammonium perfluoro(2-methyl-3-oxahexanoate) (GenX), undecafluorohexanoic acid (PFHxA), 6:2 fluorotelomer sulfonic acid (6:2 FTS, crystallized, cf. Freilinger et al., 2025b), perfluorooctanoic acid (PFOA), perfluorononanoic acid (PFNA), and perfluoro-*n*-($^{13}C_8$) octanoic acid (13C8-PFOA). Furthermore, the organic micropollutants (OMPs) 1,2,3-benzotriazole (BTZ), carbamazepine (CBM), and diclofenac sodium salt (DCF) were applied.

Materials for polymer synthesis included 3-(1*H*,1*H*,2*H*,2*H*-perfluorooctyl)-1-vinylimidazolium chloride (F-monomer, **[2126844-17-3]**, Partl et al., 2021) and the crosslinker 3,3′-(hexane-1,6-diyl)bis (1-vinylimidazolium) bromide (HVIB, **[1046127-79-0]**, Cui et al., 2014; Gelbrich et al., 2026). A list of the materials used, their specifications, and the suppliers as well as details on monomer synthesis can be found in the Supplementary materials, Section S1.

2.2. Methods

2.2.1. Polymer synthesis

The fluorinated polymer (FP-AER) **[3099590-37-8]** was synthesized by copolymerizing the F-monomer (400 mg, 0.91 equiv) with the crosslinker HVIB (400 mg, 1 equiv) in a solvent mixture of 500 mg 1-propanol, 500 mg ACN, and 200 mg H_2O. 40 mg DMPA was used as the initiator for polymerization. The formulation was sonicated for 5 min, cast between quartz plates, and irradiated with UV light (8 W, 254 nm; CX-2000 UV Crosslinker) for 30 min. The resulting precipitate was washed sequentially with water, ACN, and MeOH using a funnel filter (DURAN; porosity 3), dried overnight at 60 °C, and ground to a particle size between 50 µm and 500 µm. The final product was dried overnight at the same temperature. The copolymer can be termed as poly(3-(perfluorohexyl-ethyl)-1-vinylimidazolium-*co/ran*-3-(1,6-hexylene)-bis-1-vinylimidazolium) bromide chloride and, for short, as poly(pfC6-Et-VIm$^+$-*co*-Hx-(VIm$^+$)$_2$), where "pfC6" denotes a perfluorohexyl substituent (C_6F_{13}) according to the materials overview Table S5. In an equimolar repeat, the composition carries a net charge of +3 (one Im$^+$ in the F-monomer and two Im$^+$ units in the crosslinker), whereas for an equal-mass repeat the theoretical ion-exchange capacity is 3.36 meq g^{-1}. Each monomer contributes one perfluorohexyl segment, corresponding to 1.05 mmol g^{-1} C_6F_{13} groups in the equal-mass case.

2.2.2. Physicochemical characterization

The following techniques were applied: Scanning electron microscopy (SEM)/energy-dispersive X-ray spectroscopy (EDS), thermogravimetric analysis (TGA)/differential scanning calorimetry (DSC), attenuated total reflectance (ATR)/Fourier-transform infrared (FTIR) spectroscopy, N_2 physisorption at 77 K, laser diffraction, elemental C/H/N/S/O/F/Cl/Br analysis, X-ray photoelectron spectroscopy (XPS), determination of ion-exchange capacity. Details are provided in the Supplementary materials, Section S2.

2.2.3. PFAS adsorption assays

PFAS adsorption studies were conducted in comparison with a commercial PAC (Carbopal AP; Donau Carbon, Pischelsdorf, Austria). Single-component isotherms, multi-component isotherms, and single-component adsorption kinetics were conducted with PFOA, GenX, and PFBA at initial concentrations c_0 of 0.1 and 1 mg L^{-1}. These levels are well above drinking-water regulations but allowed us to resolve equilibrium concentrations near 50 µg L^{-1} – levels reported at some highly impacted AFFF-site groundwaters (Houtz et al., 2013). Competitive adsorption and the influence of ionic strength were evaluated in water matrices containing OMP and NaCl. We selected BTZ, CBM, and DCF as representative OMPs that commonly co-occur with PFAS in wastewater-impacted waters (Loos et al., 2013), spanning neutral polar (BTZ), neutral moderately hydrophobic (CBM), and anionic (DCF) species to probe hydrophobic and electrostatic competition. Batch screening studies further compared FP-AER with PAC, and two ion-exchange resins under matched conditions (30 mg L^{-1} adsorbent; 1 mg L^{-1} each of PFOA, PFBA, and GenX; all materials milled and conditioned identically). Exploratory rapid small-scale column tests (RSSCT) were also performed using FP-AER packed in solid-phase extraction (SPE) cartridges (1 mL, PP, with 20 µm PE frits; Merck, Darmstadt, Germany) and operated for 132 h (≈150,000 bed volumes) with 1 mg L^{-1} each of PFOA, PFBA, and GenX. The regenerability of the adsorbents was evaluated in SPE cartridges packed with 30 mg adsorbent via multiple adsorption–desorption cycles using MeOH containing 0.5 % of NH_4Cl, LiCl and FA each (w/w/v). Adsorption tests in a real water matrix were conducted using groundwater from an AFFF-impacted airport after spiking with 0.5 µg L^{-1} each of PFBA, PFBS, PFPeA, GenX, PFHxA, 6:2 FTS, PFOA, and PFNA. Details are provided in the Supplementary materials, Section S3.

2.2.4. Analytical methods

PFAS analysis using HPLC-MS/MS, OMP analysis using HPLC-UV, and ion chromatography using a Dionex IC-2500 system are described in the Supplementary materials, Section S4.

3. Results and discussion

3.1. Physicochemical characterization

The facile synthesis route produced a semifluoroalkylated polyvinylimidazolium resin (FP-AER; Fig. 1) consistent with the targeted bulk composition $[(C_{13}H_{10}N_2F_{13}Cl)_{0.91}(C_{16}H_{24}N_4Br_2)]_n$. Bulk elemental analysis (CHNS with halogens), SEM-EDS, and XPS confirm incorporation of both the fluorinated monomer and the bis-imidazolium crosslinker in the expected ratios. Despite this agreement in bulk, the tendency of hydrocarbons and perfluorocarbons to exhibit large miscibility gaps can drive fluorophilic segregation during network formation (Lai et al., 2025). In particular, the polymerization solvent–porogen composition and the content of fluorinated moieties in random copolymers strongly influence segmented-domain formation via coupled enthalpic and entropic effects (Ye et al., 2010). As expected, EDS (which does not detect hydrogen) is consistent with theoretical composition for C, F, and Br, while modest deviations in N and Cl reflect known limitations of EDS quantification for light elements and halogens. Potential fluorine-rich domains arising from F···F interactions and localized aggregation of the F-monomer may occur at the microscale but are averaged out in area-scan measurements. By contrast, bulk elemental analysis (including H) agrees with the respective theoretical composition within experimental uncertainty. XPS (surface sensitive; H not detectable) likewise shows agreement for C and F, with slightly lower N and slightly higher Cl/Br levels; the C–F_2/C–F_3 C 1 s area ratio of 5:1 matches the expected perfluoroalkyl composition (Figure S5). In general, these data support the summative stoichiometry in the polymer matrix (Fig. 2).

The proposed structure of the polymer (Fig. 1) is further supported by ATR-FTIR spectroscopy (Figure S2), which displays characteristic absorption bands at approximately 3130 cm^{-1} (aromatic C—H stretching), 2943 cm^{-1} (aliphatic C—H stretching), 1629 cm^{-1} (vinyl or conjugated aromatic C═C stretching), 1569 cm^{-1} (aromatic C═C stretching), 1551 cm^{-1} (C═N stretching). The presence of fluorinated groups is indicated by the absorption bands at approximately 1234 cm^{-1} (C-F_3 stretching vibration), 1194, 1144, 737 cm^{-1} (C-F_2 stretching vibrations). The main absorption bands observed in the spectrum are at ν = 3130, 3063, 2943, 2864, 1629, 1569, 1551, 1458, 1433, 1365, 1351, 1318, 1234, 1194, 1163, 1144, 1122, 1080, 1000, 951, 913, 842, 810, 746, 737, 724, 708 cm^{-1}. The ATR-FTIR spectra from the monomer, crosslinker, and polymer show overlapping absorption bands, consistent with the successful incorporation of both monomer and crosslinker into the polymer (Figure S2).

Scanning electron micrographs of the FP-AER (Fig. 3) reveal an open, porous morphology consistent with phase separation induced by porogens during synthesis. While such macroporous channels are expected to facilitate mass transfer of PFAS into the adsorbent, nitrogen physisorption nevertheless indicates a low BET surface area of 4.49 m^2 g^{-1} for FP-AER versus 923 m^2 g^{-1} for the activated carbon reference. CO_2 uptake at 273 K at p/p_0 = 0.03 was 9.68 cm^3 (STP) g^{-1} for FP-AER and 72.52 cm^3 (STP) g^{-1} for activated carbon (isotherms in Figure S3). These measurements suggest limited interaction of the highly fluorinated surface with standard physisorption probes and highlight that BET area does not necessarily predict PFAS adsorption capacity for tailored fluorinated sorbents (cf. Sun et al., 2026).

The thermal stability of the polymer is high: thermal decomposition initiates at approximately 265 °C under both oxidizing (air) and non-oxidizing (nitrogen) atmospheres (Figure S4). Beyond this onset, the first mass-loss event is consistent with decomposition of the imidazolium moiety, (Chavan et al., 2018; Singh et al., 2023) with DSC peak

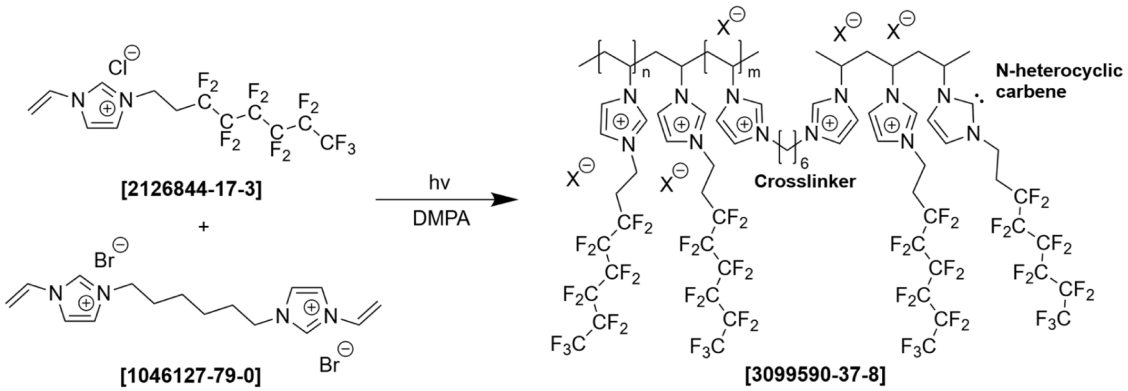

Fig. 1. Synthesis of the crosslinked fluorinated polymer (FP-AER).

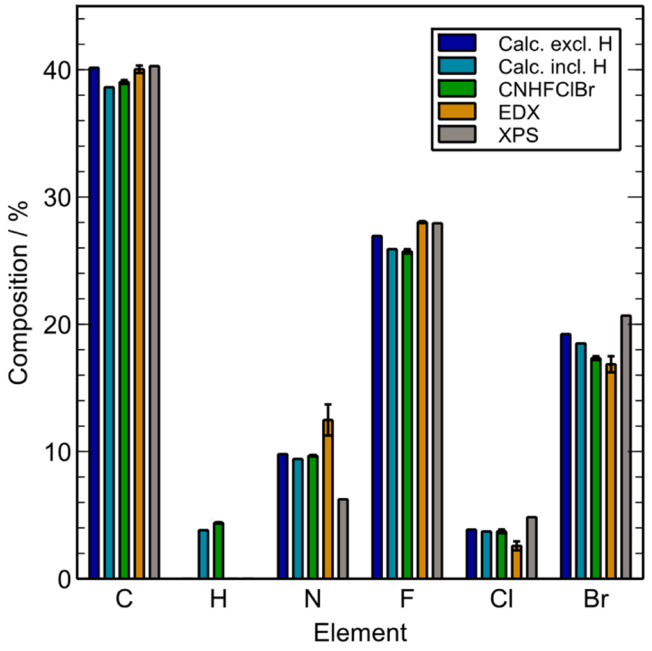

Fig. 2. Elemental composition (m/m) of FP-AER versus the targeted bulk composition $[(C_{13}H_{10}N_2F_{13}Cl)_{0.91}(C_{16}H_{24}N_4Br_2)]_n$. Theoretical mass fractions (H-included and H-excluded), SEM–EDS (H not detectable), bulk CHNS/halogen analysis, and XPS (H not detectable). Means and standard deviations shown ($n = 3$; for XPS: $n = 1$).

temperatures of 299 °C in air and 291 °C in nitrogen. The subsequent stage, with DSC peaks at 321 °C (air) and 337 °C (nitrogen), is consistent with further backbone degradation and may involve partial transformation of perfluoroalkyl segments to smaller volatile species, though a definitive assignment requires off-gas analysis. A similar two-stage decomposition was observed for materials crosslinked with EGDMA in SPE-optimized polymers (Freilinger et al., 2025a).

The fluorinated polymer exhibits substantial anion-exchange capacity, with an overall capacity of 1594 ± 75 μeq g^{-1} (mean ± SD, n = 5). The theoretical capacity, estimated from the stoichiometric Cl^- and Br^- content of the targeted repeat unit, is 3360 μeq g^{-1}, indicating that approximately 47 % of the nominal sites are accessible under the measurement conditions. This shortfall likely reflects partial site occlusion within the crosslinked network, steric shielding and limited swelling of the fluorinated matrix, and/or incomplete displacement during the exchange protocol.

3.2. PFAS adsorption performance

3.2.1. Isotherms

Single- and multi-component isotherms for PFOA, GenX, and PFBA on the FP-AER and the reference PAC are well described by both Langmuir and Freundlich models across the investigated concentration range (Fig. 4, Table S1). The sole exception is PFBA on FP-AER, which exhibits an approximately linear isotherm under our conditions and is therefore better represented by the Freundlich model; saturation was not reached, yielding unrealistically high extrapolated Langmuir capacities.

In single-component tests, FP-AER attains Langmuir maximum loadings of 597 mg g^{-1} (1440 μmol g^{-1}) for PFOA and 143 mg g^{-1} (433 μmol g^{-1}) for GenX, while PFBA is characterized by a Freundlich constant of 22.3 $mg^{1-(1/n)}$ $L^{1/n}$ g^{-1} (Table S1). Relative to PAC, FP-AER shows substantially higher uptake: 12-fold for PFOA and 5.1-fold for GenX based on Langmuir capacities, and a 6.2-fold higher Freundlich constant for PFBA (Fig. 4a–c; Table S1). These data indicate strong capacity and affinity on FP-AER with a pronounced chain-length dependence favouring long-chain PFAAs.

To evaluate performance at concentrations observed in affected waters, we probed the low-concentration isotherm window by combining two initial concentration levels (0.1 and 1 mg L^{-1}), achieving a variable number of c_{eq} datapoints below 0.08 mg L^{-1} (Figure S6). At a common reference point of c_{eq} = 50 μg L^{-1} (a comparative benchmark well above drinking-water targets but within ranges reported at a highly impacted AFFF training site; Houtz et al., 2013), the average of the Langmuir- and Freundlich-based predictions yields, for single-solute conditions, loadings on FP-AER versus PAC of 237 vs 26.0 mg g^{-1} for PFOA, 24.8 vs 6.7 mg g^{-1} for GenX, and 0.95 vs 0.48 mg g^{-1} for PFBA. Under multi-solute conditions at the same c_{eq}, FP-AER maintains pronounced advantages for all three PFAS, most notably for PFOA. Notably, FP-AER sustains high PFOA uptake (204 mg g^{-1}) at c_{eq} = 50 μg L^{-1}, outperforming PAC by factors of approximately 6–9 even under multi-solute conditions; GenX advantages remain 3–5-fold, while PFBA maintains modest but consistent advantages.

Under multi-component conditions with all three PFAS present (full isotherms in Fig. 4d–F), FP-AER exhibits a Langmuir maximum loading of 466 mg g^{-1} for PFOA and 66.7 mg g^{-1} for GenX, and a Freundlich constant of 9.29 $mg^{1-(1/n)}$ $L^{1/n}$ g^{-1} for PFBA (Table S1). Compared to single-component systems, the reductions are 21.9 % for PFOA, 53.4 % for GenX, and 42.7 % for PFBA, consistent with competitive adsorption and preferential occupation of high-affinity domains by the long-chain PFAS. Displacement of GenX and PFBA becomes more apparent at higher equilibrium concentrations, supporting the higher affinity of PFOA for FP-AER. PAC shows a similar qualitative trend but with stronger decreases in adsorption metrics and a pronounced bias toward long-chain PFAS, consistent with prior observations (McCleaf et al., 2017; Riegel et al., 2023). In direct FP-AER–PAC comparisons within

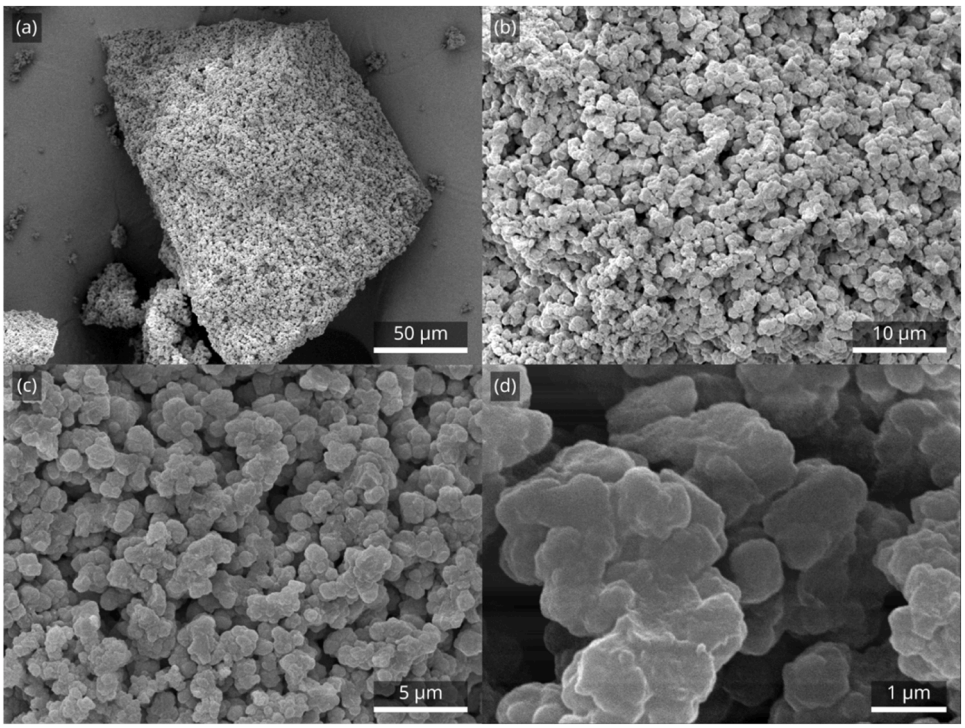

Fig. 3. Scanning electron micrographs of unmilled FP-AER.

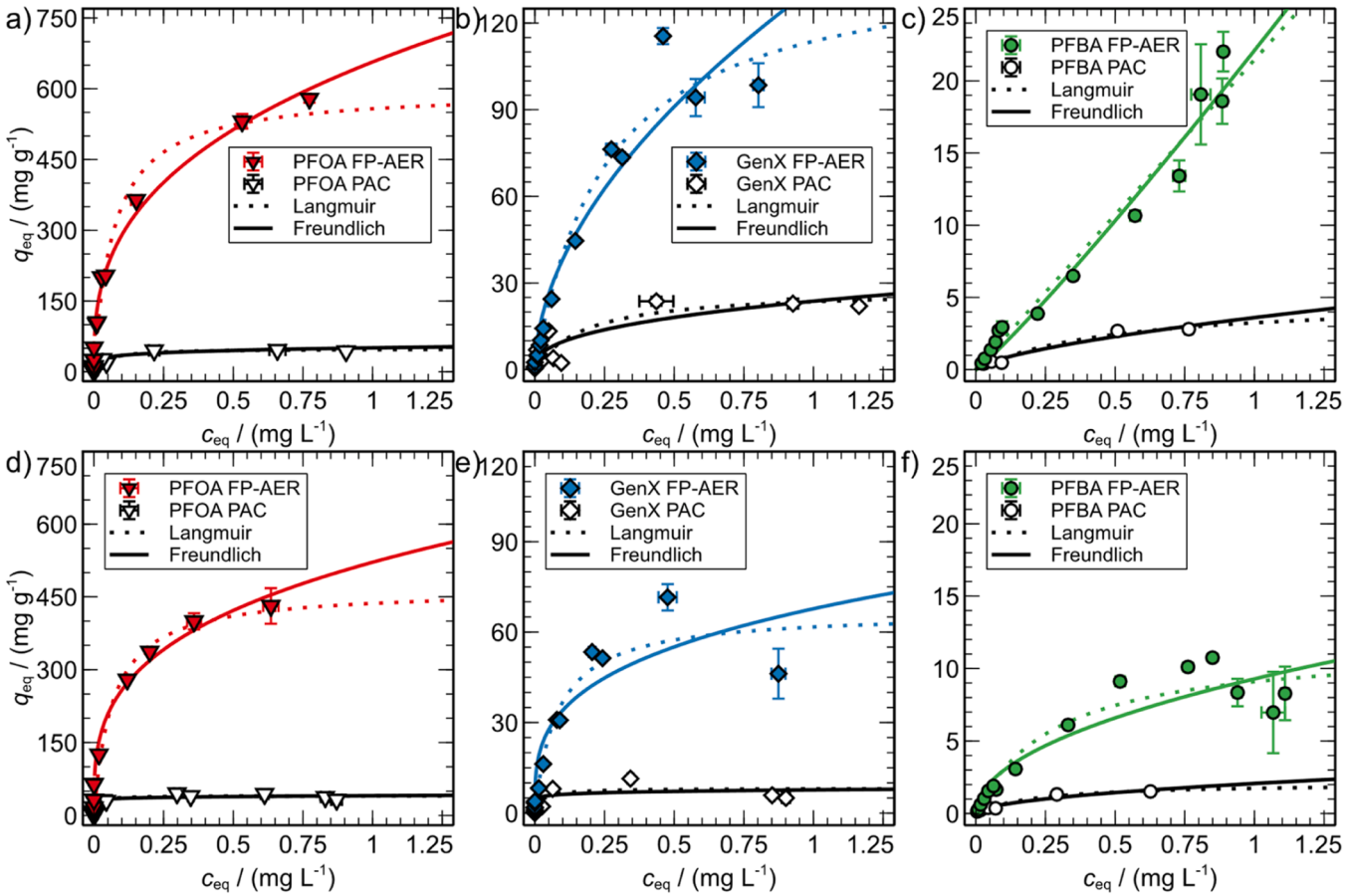

Fig. 4. PFAS isotherms on FP-AER and PAC including respective Langmuir and Freundlich regressions. a), b), c): Single-component isotherms for perfluorooctanoic acid (PFOA), hexafluoropropylene oxide dimer acid (GenX), perfluorobutanoic acid (PFBA). d), e), f): Multi-component isotherms. Fit parameters and 95 % confidence intervals given in Table S1. Low-concentration performance (c_{eq} <0.08 mg L^{-1}) shown in Figure S6. Means and standard deviations shown (n = 3).

mixed-solute systems, FP-AER continues to outperform PAC, with single-solute loading equivalents that are 11.5-fold (PFOA) and 8.16-fold (GenX) higher, and a 4.49-fold higher Freundlich constant for PFBA (Fig. 4d–F; Table S1). Taken together with the low-concentration analysis (Figure S6), these results establish that FP-AER delivers high capacities and maintains a clear advantage over PAC down to c_{eq} levels observed in affected waters and in competitive mixtures, motivating the mechanistic discussion and literature benchmarking presented in Section 3.2.6. Note that Langmuir/Freundlich parameters in mixtures are empirical, used here for comparison; rigorous multicomponent predictions would require, e.g., IAST (ideal adsorbed solution theory) modelling. Exploratory batch screening with two commercial PFAS-selective AERs under the same conditions showed similar performance to FP-AER (Figure S9). While informative for material screening at elevated c_0 in ideal matrices, these tests are not representative of drinking-water treatment and warrant further investigation under continuous-flow operation and lower influent levels.

3.2.2. *Kinetics and column tests*

The time-dependent uptake of PFOA, GenX, and PFBA on FP-AER and PAC was quantified under single- and multi-component conditions (Fig. 5; Table S2). For FP-AER, PFOA kinetics are best approximated by the pseudo-first-order model, while GenX and PFBA are better captured by pseudo-second-order fits; in all cases, adsorption approaches equilibrium within 24 h for both single and mixed systems. In contrast, PAC kinetics are consistently described more accurately by pseudo-first-order fits for all three PFAS, and none of the analytes reach clear equilibrium within 48 h under either single- or multi-component conditions.

Particle size differences contribute to, but do not fully explain, the kinetic contrast. After milling, the median particle sizes d_{50} were 5.0 µm for FP-AER and 15.3 µm for PAC (Figure S1). If intraparticle diffusion dominates, characteristic equilibration times scale approximately with the square of the diffusion path length, $t \propto L^2/D_{eff}$; thus, the approximately three-fold larger diameter of PAC implies on the order of a roughly nine-fold longer diffusion time relative to FP-AER, all else equal (Ruthven, 1984). However, the observed behaviour reflects more than particle size: FP-AER's rapid approach to steady state and higher asymptotic loadings are consistent with its open, macroporous morphology (Fig. 3), low microporosity (physisorption, Figure S3), and fluorinated, PFAA-affine surfaces, which together reduce internal diffusion constraints and facilitate access to adsorption domains. Conversely, PAC exhibits slower, near-linear increases in q without clear plateaus within 48 h, indicative of significant intraparticle diffusion resistance within a predominantly microporous structure despite the agitation conditions used. External (film) mass-transfer limitations are expected to be minor under the applied mixing, and the smaller FP-AER particles would further diminish film resistance; nonetheless, the persistence of slower PAC uptake strongly implicates internal diffusion as the rate-limiting step for PAC.

Competition in the multi-component experiments slightly slows the

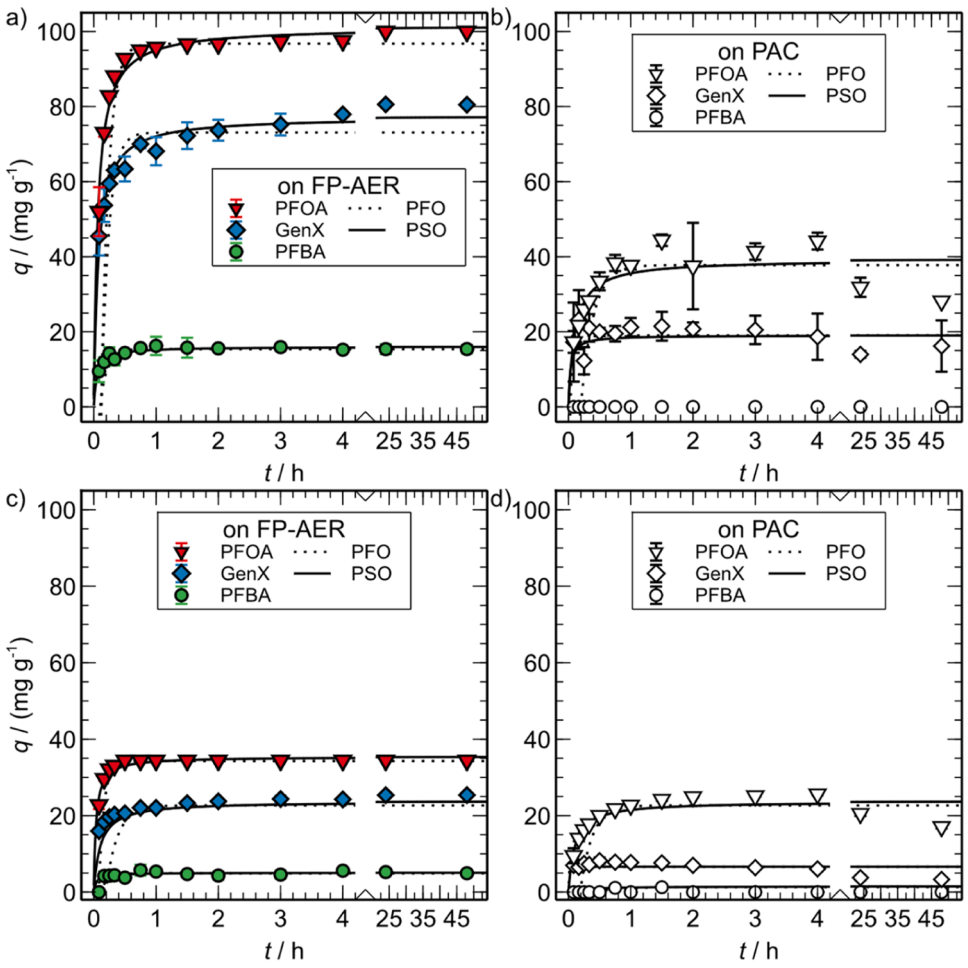

Fig. 5. Adsorption kinetics of perfluorooctanoic acid (PFOA), hexafluoropropylene oxide dimer acid (GenX), and perfluorobutanoic acid (PFBA) on 10 mg L^{-1} of the adsorbents FP-AER (a, c) and PAC (b, d), respectively, using a single PFAS (c_0 = 1 mg L^{-1}) (a, b) or a mixture of all three PFAS (c_0 = 0.33 mg L^{-1} of each PFAS) (c, d) including respective pseudo-first order (PFO) and pseudo-second order (PSO) regressions. Fit parameters and 95 % confidence intervals given in Table S2. Means and standard deviations shown (n = 3).

approach to equilibrium on FP-AER and depresses the asymptotic loading for GenX and PFBA relative to PFOA, mirroring the chain-length selectivity observed in the isotherms. While the pseudo-first- and pseudo-second-order fits serve as empirical descriptors rather than mechanistic rate laws, the consistent patterns – faster equilibration and higher asymptotic loadings on FP-AER despite smaller diffusion path lengths being only part of the explanation – underscore the combined effects of favourable transport pathways and stronger effective affinity on the fluorinated polymer. However, because part of the apparent kinetic advantage may arise from residual particle-size differences, practical implications should be drawn cautiously and ideally verified under matched size distributions and fixed-bed conditions. Taken together, the kinetic results reinforce FP-AER's potential practical advantage over PAC by enabling near-complete utilization of adsorption capacity within 24 h, even in competitive mixtures.

To probe performance under flow, we conducted exploratory RSSCTs with FP-AER (Figure S10). Despite the elevated influent concentration (1 mg L^{-1} per PFAS), the columns showed clear separation in breakthrough: PFBA broke through rapidly (≈ 7000 BV at 50 % breakthrough) with a well-documented chromatographic displacement pattern above $c/c_0 = 1$ (e.g., Riegel et al., 2023); GenX exhibited intermediate breakthrough (≈ 53,000 BV), while PFOA increased only slowly without reaching significant breakthrough over 141,000 BV. Estimated particle Peclet (Re×Sc) numbers were 390–680 for the PFAS tested, indicating laminar flow with thin external films and intraparticle diffusion likely dominates the mass-transfer resistance. The Thomas model provided adequate empirical fits to the breakthrough data (except PFOA), consistent with prior applications to PFAS adsorbents (e.g., Pannu et al., 2023). Notably, the sustained PFOA removal by FP-AER is promising; typical column tests report PFOA breakthrough earlier at much lower ng L^{-1}–µg L^{-1} levels – for example, granular activated carbon (GAC) RSSCTs showed significant PFOA breakthrough ranging from 20,000 to 65,000 BV in some matrices, with others exceeding 120,000 BV (matrix- and adsorbent-dependent; Pannu et al., 2023), while recent pilot-scale tests reported values of approximately 124,000–377,000 BV across several AER and alternative adsorbents (Pannu et al., 2024). More detailed transport analysis (e.g., constant vs. proportional diffusivity RSSCT frameworks; Crittenden et al., 1986, 1987, mass-transfer resistances) would benefit from an expanded dataset; future work will vary hydraulic loading rate and particle size and lower feed concentrations to enable rigorous scaling (cf. Cheng and Knappe, 2024) and more robust interpretation. Overall, these results demonstrate that FP-AER also performs effectively in column mode.

3.2.3. *Effects of co-solutes and ionic strength*

Varying concentrations of OMPs in the matrix do not measurably influence the adsorption of PFOA, GenX, or PFBA on the FP-AER (Fig. 6a). In contrast, on PAC the equilibrium loading of PFOA declines markedly as OMP concentration increases (Fig. 6b), indicating higher selectivity of FP-AER for the three PFAS compared to PAC. FP-

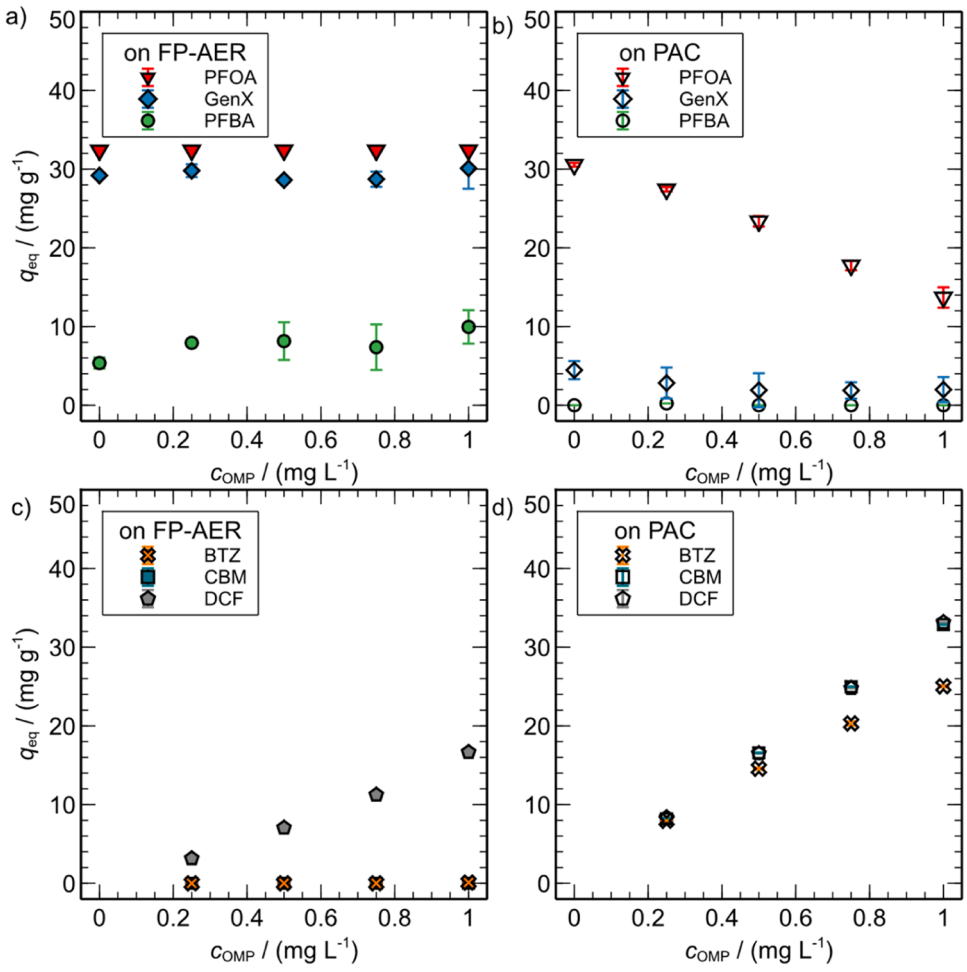

Fig. 6. Competitive adsorption of perfluorooctanoic acid (PFOA), hexafluoropropylene oxide dimer acid (GenX), perfluorobutanoic acid (PFBA) and the organic micropollutants (OMPs) benzotriazole (BTZ), carbamazepine (CBM) and diclofenac (DCF) on 30 mg L^{-1} of adsorbent: FP-AER (a, c) and PAC (b, d). Experiments used mixtures containing all three PFAS and all three OMPs with initial concentrations $c_0 = 1$ mg L^{-1} for each PFAS; initial OMP concentrations were varied as indicated. Means and standard deviations shown ($n = 3$).

AER shows no detectable uptake of BTZ or CBM, and only slight uptake of DCF, attributable to anion exchange (Fig. 6c). PAC adsorbs all three OMPs, with slightly higher affinity toward the larger molecules CBM and DCF (Fig. 6d).

Ionic strength exerts opposing effects on the two adsorbents. On FP-AER, chloride competes with PFAAs at cationic sites, and increasing NaCl concentration decreases the equilibrium loadings of PFOA, GenX, and PFBA (Figure S7a). On PAC, PFOA loading increases with ionic strength (Figure S7b), consistent with a salting-out effect that reduces aqueous PFAA activity and promotes adsorption (reported previously for PFOS; cf. Li et al., 2022). We note that salting out likely also influences PFOA on FP-AER at higher NaCl levels, where FP-AER loadings approach those of PAC under the same high-salt conditions; PFBA shows tentative increases at NaCl concentrations $\geq$350 mg L^{-1} and remains near zero, with larger error bars suggesting the onset of weak salting-out effects.

When OMPs and salt are present together, FP-AER exhibits reduced loadings of PFOA, GenX, and PFBA with increasing NaCl, reflecting additive competition from chloride alongside inert/weakly adsorbing OMPs and salting-out effects of varying strength (strong for PFOA, onset/weak for GenX and PFBA; Figure S8a). On PAC, PFOA loading increases with NaCl even in the presence of OMPs due to salting-out effects (Figure S8b), yet the maximum PFOA loading on PAC remains lower than on FP-AER across the conditions tested. FP-AER's superior PFAA selectivity in OMP-containing matrices is maintained (Figure S8vs b). For FP-AER, DCF adsorption declines with increasing NaCl (Figure S8c), consistent with competitive uptake of chloride at anion-exchange sites. On PAC, NaCl does not affect OMP adsorption (Figure S8d), consistent with predominantly hydrophobic interactions as the governing mechanism. It is acknowledged that chloride sensitivity constitutes a potential operational limitation, as elevated chloride (and ionic strength) can reduce working capacity/selectivity; this should be accounted for in design and water-matrix selection (e.g., high-chloride or softened/brackish sources) and will be addressed in future optimization.

3.2.4. *Desorption efficiency*

Our objective was to demonstrate the reversibility of PFAS adsorption on FP-AER. The small particle size precluded reproducible cycle-to-cycle separation by centrifugation after each loading step, so regeneration tests were conducted in cartridge format. In this configuration, experiments were not run to saturation; consequently, we cannot directly compare absolute capacities before and after each regeneration cycle. We therefore report cycle-wise desorption recoveries and qualitative reproducibility.

Under these conditions, FP-AER consistently achieved high elution recoveries (>90 %) for both short- and long-chain PFAS across six cycles (Fig. 7). PAC exhibited pronounced variability between cycles, especially for short-chain PFAS (PFBA: 50.8–79.0 %; GenX: 27.0–62.4 %). The SPE setup allows controlled desorption and mass balance, but does not capture fixed-bed hydrodynamics or quantify pre/post-cycle working-capacity retention, and thus is not a substitute for fixed-bed cycling. Nonetheless, several lines of evidence suggest FP-AER capacity remains essentially unchanged over the tested cycles: (i) high and stable recoveries indicate minimal irreversible adsorption; (ii) post-regeneration uptake at low coverage (i.e., below saturation) shows no measurable decline across cycles; and (iii) the fluorous, macroporous matrix and cationic sites are chemically robust under the regeneration conditions employed. In contrast, PAC's lower and more variable recoveries are consistent with micropore trapping and hysteresis.

These observations align with a broader literature consensus that alcohol–salt eluents are the most reliable regenerants for PFAS-laden adsorbents and ion-exchange media. Boyer et al. (2021) concluded that methanol/salt mixtures provide the most consistent regeneration performance across material classes. Butzlaff et al. (2025) showed that a mixed methanol–ammonium acetate eluent regenerated a commercial

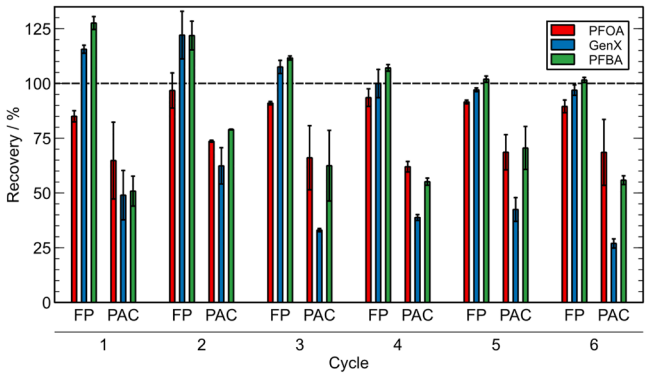

Fig. 7. Regeneration of the PFAS perfluorooctanoic acid (PFOA), hexafluoropropylene oxide dimer acid (GenX), perfluorobutanoic acid (PFBA) from FP-AER and PAC in cartridge tests using a mixture of all three PFAS at 100 µg L^{-1} each. After loading with 1 mL and a rinse with MeOH/water (1:9, v/v), desorption was performed as a flow-through step (compressed air, 1 bar) with 1 mL methanol containing 0.5 % (w/w/v) each of NH_4Cl, LiCl, and formic acid. Shown are recoveries (%) – defined as desorbed PFAS relative to the adsorbed amount in that cycle – for each PFAS across six regeneration cycles and both adsorbents. Means and standard deviations shown ($n = 3$).

PFAS-selective ion exchanger (Purolite PFA694E) far more effectively than methanol or ammonium acetate alone, highlighting the synergy of an organic modifier with a competing counterion. Ellis et al. (2025) systematically varied solvent–brine compositions and found that methanol–brine solutions effectively regenerate both "regenerable" and "PFAS-selective/single-use" resins using 10–30 bed volumes, with up to 90 % methanol recovery by distillation; the residual PFAS-concentrated fraction can be managed off-site (e.g., high-temperature destruction). Their life-cycle assessment indicated low environmental impact and favourable costs when solvent recovery is implemented. Mechanistically, methanol disrupts hydrophobic/fluorous interactions and hydrogen bonding that retain PFAS, while added salt screens electrostatics and provides counterions that displace anionic PFAAs from cationic sites (Boyer et al., 2021; Butzlaff et al., 2025; Ellis et al., 2025).

In FP-AER, the cationic binding sites are quaternized vinylimidazolium groups. Under strongly basic conditions, these can, in principle, undergo C2–H deprotonation to form transient imidazole-2-ylidenes (N-heterocyclic carbenes, NHCs; Fig. 1, rightmost heterocycle). Tertiary amines (e.g., triethylamine) can promote this, and even acetate can act as a moderate base under suitable media to form NHCs (Gurau et al., 2011). However, under our alcohol–salt regeneration conditions (methanol with neutral salts and FA; not basic), NHC formation is not expected and is evidently unnecessary for effective regeneration (Fig. 7). Conceptually, transient neutralization of imidazolium sites via C2–H deprotonation would weaken electrostatic PFAA–FP-AER interactions and could promote desorption, but accessing this chemistry would require strongly basic, largely aprotic media.

Accordingly, our regeneration strategy emphasizes alcohol–salt eluents rather than base-driven speciation of imidazolium sites. From an implementation perspective, the use of neat or high-fraction methanol necessitates closed-loop handling, appropriate fire safety measures (including explosion-proof equipment), and solvent recovery to minimize cost and environmental burdens. Incorporating distillation for solvent recovery, as demonstrated by Ellis et al. (2025), markedly improves life-cycle performance; the remaining small, concentrated PFAS waste stream is suitable for specialized destruction.

Future work will quantify capacity retention by conducting full breakthrough/saturation–regeneration cycles in fixed beds (e.g., using immobilized FP-AER to enable complete saturation and direct pre/post comparison), complemented by material characterization before and after cycling.

3.2.5. Performance in AFFF-Impacted groundwater

To evaluate performance in an application-near yet controlled matrix, we used groundwater from an AFFF-impacted site (pH = 8.02, conductivity = 479 µS cm^{-1}, and NPOC = 2.12 mg L^{-1}) and spiked a defined PFAS spectrum comprising perfluoroalkyl carboxylates of varying chain length (PFBA, PFPeA, PFHxA, PFOA, PFNA), a perfluoroalkyl sulfonate (PFBS), a fluorotelomer sulfonate (6:2 FTS), and a perfluoroether carboxylate (GenX), each at c_0 = 0.5 µg L^{-1}. The control (spiked) reflects native background plus spike and shows elevated PFHxA, PFOA, and PFNA (and PFBA), typical of AFFF-impacted matrices (Table S3).

Batch tests at adsorbent doses of 5 and 10 mg L^{-1} showed that FP-AER outperformed PAC across the spiked mixture (Fig. 8; Table S3). Averaged over all targeted PFAS, removals were 91.7 % (FP-AER) vs 67.6 % (PAC) at 5 mg L^{-1}; and 94.1 % (FP-AER) vs 73.7 % (PAC) at 10 mg L^{-1}. Because PAC exhibited apparent negative removal for PFBA – likely due to blank value or procedural/background contamination – we also report PFBA-excluded averages: 96.2 % (FP-AER) vs 81.4 % (PAC) at 5 mg L^{-1}, and 97.4 % (FP-AER) vs 93.1 % (PAC) at 10 mg L^{-1}. Cross-contamination is especially common for PFBA due to its ubiquity and high mobility (Lin et al., 2023; Roberts et al., 2023). These results confirm FP-AER's advantage at environmentally relevant concentrations, particularly at the lower dose and when short-chain species are included.

We focused on anionic PFAAs as the persistent end-products of AFFF weathering and the species that typically dominate AFFF-impacted groundwater (Houtz et al., 2013). This choice also aligns with the intended dual-mode mechanism of FP-AER – electrostatic binding at imidazolium sites coupled with fluorophilic tail interactions – which targets anionic fluorosurfactants most directly. While current regulations emphasize PFAAs (e.g., European Parliament, 2020), we acknowledge that zwitterionic and cationic PFAS, as well as hydrocarbon surfactants, can occur in AFFF-impacted waters (Houtz et al., 2013). Although electrostatic repulsion from the cationic FP-AER matrix may disfavour cationic/zwitterionic headgroups, the fluorophilic domains may still promote partitioning via tail interactions; quantifying such uptake will be the subject of future studies.

3.2.6. Adsorption mechanism and literature benchmarking

FP-AER's performance arises from three cooperative interactions: electrostatic binding at densely distributed imidazolium sites (3.36 mmol Im^+ g^{-1}), F···F interactions of PFAA tails via ethylene-linked perfluorohexyl groups (1.05 mmol C_6F_{13} g^{-1}) positioned near the cation, and subordinate hydrophobic contributions from the aliphatic backbone/crosslinker. Normalizing single-component capacities to these moieties shows no clear one-to-one scaling: While PFOA corresponds to 0.43 molecules per Im+ and 1.37 per C_6F_{13} segment (single-solute Langmuir capacities), a strong chain-length related drop is observed for GenX and PFBA (Table S1). Yet, in contrast to random copolymers of separate charged and fluorinated monomers (e.g. Chavan et al., 2018), FP-AER covalently co-localizes the imidazolium and the perfluorohexyl segment within the same repeat unit (via an ethylene linker), ensuring head–tail complementarity at every site and yielding consistently high apparent affinity and capacity. Selectivity reflects strong interactions with PFAAs but weak interactions with NOM/OMPs (Fig. 6), while competition with anions (notably Cl^-) enables efficient alcohol-salt regeneration (Fig. 7).

Relative to "standard" anion-exchange resins (AERs), a review median of 1550 µmol g^{-1} translates to approx. 640 mg g^{-1} for PFOA (Dixit et al., 2021), although cross-study variability in experimental conditions, in particular initial concentration c_0 and equilibrium concentration c_{eq}, limits comparability. Our isotherms span a range of c_0 = 0.1–1 mg L^{-1} with c_{eq} often below 0.08 mg L^{-1} (Figure S6), where FP-AER reaches q_{max} = 597 mg g^{-1} (PFOA) and 143 mg g^{-1} (GenX) and maintains high mixed-solute performance (Section 3.2.1). The most comparable commercial PFAS-selective resin (Purolite PFA694E) reports 97 mg g^{-1} for PFOA at c_{eq} of approx. 8 mg L^{-1} (single-point from log K_d) (Butzlaff et al., 2025), well below FP-AER at much lower c_{eq}.

To facilitate benchmarking, we compile side-by-side literature data of emerging fluorinated sorbents (Table S5). Reported capacities span orders of magnitude and depend strongly on test windows; for instance, PFHxA values as high as 1667 mg g^{-1} at up to 300 mg L^{-1} with electrolyte (Román Santiago et al., 2023) likely reflect contributions beyond stoichiometric site binding and are obtained at concentrations far from environmental relevance. When restricting to at least broadly comparable c_{eq} windows below 10 mg L^{-1}, the next-highest Langmuir capacity is reported for a β-cyclodextrin-based quaternary ammonium-modified adsorbent crosslinked by decafluorobiphenyl (β-CD-DFB-NH—N^+) at 393 mg g^{-1} for PFOA (Sun et al., 2026), which the authors attribute to synergistic fluorophilic, hydrophobic, and electrostatic interactions on a low-surface-area, quaternized resin. Notably, Sun et al. also demonstrated direct treatment of a diluted AFFF matrix (approx. 1.3 mg L^{-1} total PFAS across 95 species) with 96.6 % total PFAS mass removal, including 88.5 % removal of zwitterionic PFAS – highlighting the benefit of combining fluorous moieties with cationic functionality in complex mixtures. In contrast, FP-AER achieves higher Langmuir capacities within similar c_{eq} ranges, which we attribute to its higher fixed-charge and site densities on a fully organic framework and its dual-mode mechanism (electrostatic/fluorophilic). Moreover, FP-AER maintains similarly strong performance at environmentally relevant

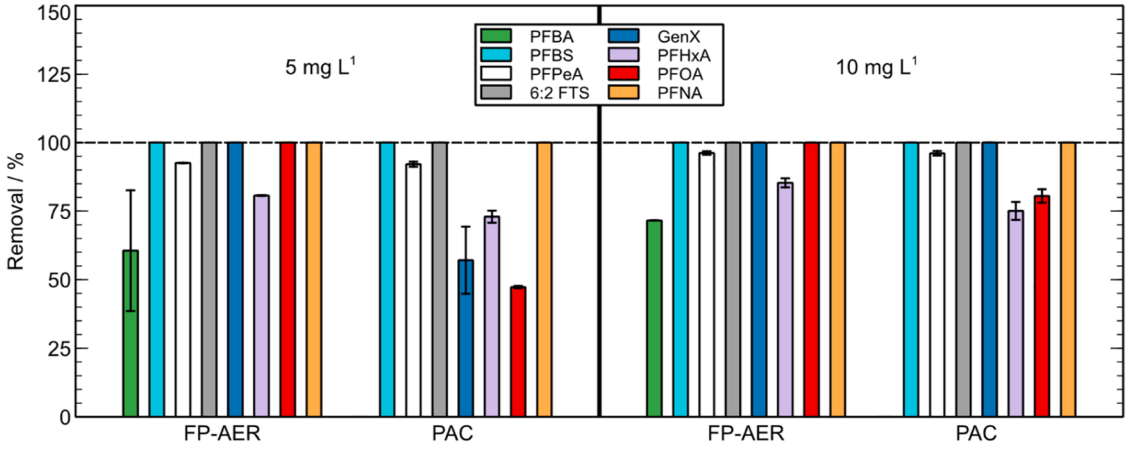

Fig. 8. Batch removal of spiked PFAS from AFFF-impacted groundwater using FP-AER and PAC. The PFAS spectrum comprised PFBA, PFBS, PFPeA, 6:2 FTS, GenX, PFHxA, PFOA, and PFNA at spiked c_0 = 0.5 µg L^{-1} each. Adsorbent doses were 5 and 10 mg L^{-1}. Concentrations given in Table S3. Means and standard deviations shown (n = 3).

concentrations in spiked AFFF-impacted groundwater, albeit demonstrated with a less elaborate analytical framework. A consistent trend is superior performance for materials that co-present fluorous moieties and cationic functionality (e.g. Huang et al., 2018; Kumarasamy et al., 2020; Manning et al., 2022; Pezoulas et al., 2025; Singh et al., 2023; Sun et al., 2026; Tan et al., 2022a; Xie et al., 2022; Yang et al., 2020) versus uncharged fluorinated networks (e.g. Huang et al., 2025; Koda et al., 2015; Quan et al., 2020; Tan et al., 2021; Xiao et al., 2017). The closest structural analogue, a silica-anchored imidazolium termed "fluor-mop" (FMV8), achieves up to 223 mg g^{-1} (PFOS) at sub-mg L^{-1}–few mg L^{-1} c_{eq} (Singh et al., 2023); FP-AER provides a higher site density through its fully organic backbone.

Durability is critical: hydrolysable linkages (e.g., siloxanes, esters, ethers; cf. Salahudeen et al., 2024; Silva et al., 2023; Wadsö and Karlsson, 2013) or labile inorganic supports risk performance loss and even leaching of fluorinated fragments. FP-AER's hydrolytically robust polyethylene backbone mitigates these risks. Moreover, even if C2–H deprotonation were to transiently form NHCs, the perfluoroalkyl substituent remains covalently tethered to the vinylimidazolium unit, and any NHC or NHC-adducts (e.g., CO_2 carboxylates) would be rapidly quenched in protic (aqueous/alcoholic) media, reforming the imidazolium (Hollóczki et al., 2011). Thus, cleavage of fluorinated fragments is not expected under our conditions. Designs that add aromatic stabilization or robust crosslinking in ionic fluorogels/porous polymer networks (Manning et al., 2022; Pezoulas et al., 2025) improve stability but, at low c_{eq}, generally report lower capacities than FP-AER.

Only a few nonpolymeric fluorinated materials have been tested near treatment-relevant levels (<10 mg L^{-1}): a polymer–MOF composite (3.6 mg g^{-1}; Ilić et al., 2025; see other fluorinated MOFs in Chen et al., 2015; He et al., 2022), fluorinated montmorillonite (81 mg g^{-1}; Du et al., 2016; see other fluorinated inorganic materials in Min et al., 2022), and a fluorine-doped mesoporous carbon (1 mg g^{-1}) (Medha et al., 2024) (see other fluorinated carbonaceous materials in Wang et al., 2018). Of these, only fluorinated montmorillonite approaches meaningful uptake and still trails FP-AER. Overall, co-localized fluorous and cationic domains in FP-AER create matched sites: electrostatic stabilization of the headgroup and F···F stabilization of the tail. This dual-mode binding explains FP-AER's high capacities and chain-length selectivity (PFOA > GenX > PFBA), resilience to OMPs, controlled sensitivity to anions, and efficient regeneration – yielding a performance envelope that compares favourably to both conventional AERs and newer fluorinated sorbents under water-treatment-relevant conditions.

4. Conclusion and outlook

This work introduces a hydrolytically robust fluorinated polymer-based anion exchange resin (FP-AER) that intrinsically co-localizes cationic imidazolium sites and ethylene-linked perfluoroalkyl moieties within each operative functionality. Across single- and multicomponent assays, FP-AER exhibits remarkable PFAA affinity and capacity with pronounced chain-length selectivity, maintains performance in the presence of organic micropollutants, yet shows pronounced sensitivity to ionic strength due to competition at cationic sites alongside fluorophilic F···F interactions and modest hydrophobic contributions. Cartridge tests demonstrate efficient and reproducible regeneration over multiple cycles using straightforward alcohol–salt eluents, consistent with a reversible dual-mode mechanism and supported by literature on solvent-brine strategies.

The accompanying mini-review and benchmarking indicate that FP-AER is competitive with both conventional anion-exchange resins and emerging fluorinated sorbents at low PFAS equilibrium concentrations relevant to highly impacted AFFF sites and in competitive mixtures. In contrast to materials relying on stochastic proximity of charged and fluorinated segments or on hydrolysis-prone scaffolds, FP-AER's architecture creates matched binding sites for PFAAs – electrostatic attraction with the headgroup and fluorophilic interaction with the tail – and a fully aliphatic backbone, which together provide a combination of selectivity, capacity, and durability while mitigating leaching risks.

Future work will transition from the present batch studies and exploratory rapid small-scale column evaluations to optimized fixed-bed operation in direct comparison with commercial PFAS-selective AERs and GAC, quantify capacity retention and breakthrough behaviour under repeated saturation–regeneration cycling, refine bed-volume-normalized regeneration with solvent recovery, and evaluate long-term stability in realistic matrices with variable NOM and background electrolytes. In parallel, we will assess process-intensified implementations – slurry adsorbers coupled with micro-/ultrafiltration membranes – to exploit FP-AER's small particle size and fast kinetics while enabling rapid solid–liquid separation, compact footprints, and closed-loop regeneration. These efforts will support rigorous techno-economic and life-cycle assessments; although per-kilogram costs will likely exceed commodity PAC at early scale, FP-AER is positioned as a PFAS-selective complement in lead/lag configurations rather than a direct substitute, with potential lifecycle advantages from high selectivity at low concentrations and regenerable operation pending scale-up and process integration. More broadly, the materials science of fluoroorganic sorbents – from task-specific HPLC polymers to fluorous AERs – targets high accessible surface area and rapid mass transfer via uniform, compact networks; in this context, we will explore fluoroalkyl-tethered vinylimidazolium crosslinkers to tune head–tail proximity, suppress fluorophilic segregation, and quantify resulting changes in capacity and kinetics.

CRediT authorship contribution statement

Judith Schobel: Writing – original draft, Visualization, Methodology, Investigation. **Johanna Freilinger:** Writing – original draft, Methodology, Investigation. **Jana Marx:** Methodology. **Madeleine Larch:** Investigation. **Martin Spruck:** Resources. **Raphael Plangger:** Investigation. **Marco Rupprich:** Project administration, Funding acquisition. **Herwig Schottenberger:** Writing – review & editing, Resources, Conceptualization. **Christian W. Huck:** Supervision, Resources. **Rania Bakry:** Supervision, Funding acquisition, Conceptualization. **Jan O. Back:** Writing – review & editing, Supervision, Project administration, Funding acquisition, Formal analysis, Conceptualization.

Declaration of competing interest

The authors declare the following financial interests/personal relationships which may be considered as potential competing interests:

Marco Rupprich, Herwig Schottenberger report a relationship with AirPlus Ltd. that includes: equity or stocks. Johanna Freilinger, Rania Bakry, Herwig Schottenberger, Marco Rupprich have patent #WO2025191130A1; EP4616941A1 pending to AirPlus Ltd. If there are other authors, they declare that they have no known competing financial interests or personal relationships that could have appeared to influence the work reported in this paper.

Acknowledgements

This work was part of the project PFAS-Trap (Project number C220002), funded by the Federal Ministry Republic of Austria, Climate Action, Environment, Energy, Mobility, Innovation and Technology. This work was co-funded by the European Union through the Interreg VI-A Austria–Germany/Bavaria 2021–2027 Programme (ERDF), project PFASelect (Grant No BA0100270). Furthermore, we thank Rodoshi Ahmed, Benedikt Aumeier, and Jörg E. Drewes from Technical University of Munich for insightful discussions.

Supplementary materials

Supplementary material associated with this article can be found, in the online version, at doi:10.1016/j.watres.2026.126201.

Data availability

Data will be made available on request.

References

Boyer, T.H., Fang, Y., Ellis, A., Dietz, R., Choi, Y.J., Schaefer, C.E., Higgins, C.P., Strathmann, T.J., 2021. Anion exchange resin removal of per- and polyfluoroalkyl substances (PFAS) from impacted water: a critical review. Water Res. 200, 117244.

Butzlaff, A.H., Mezgebe, B., Collins, A., Lin, Z.-W., Lassalle-Vega, D., Harmody, I.M., Coronell, O., Leibfarth, F.A., Dichtel, W.R., Nadagouda, M., Ateia, M., 2025. Comparative evaluation of PFAS-selective adsorbents in hard-to-treat residual waste streams. Chem. Eng. J. 511, 161983.

Chavan, S.N., Padhan, A.K., Mandal, D., 2018. Self-assembly of fluorous amphiphilic copolymers with ionogels and surface switchable wettability. Polym. Chem. 9 (17), 2258–2270.

Chen, T.-H., Popov, I., Kaveevivitchai, W., Chuang, Y.-C., Chen, Y.-S., Jacobson, A.J., Miljanić, O.Š., 2015. Mesoporous fluorinated metal-organic frameworks with exceptional adsorption of fluorocarbons and CFCs. Angew. Chem. Int. Ed. 54 (47), 13902–13906.

Cheng, L., Knappe, D.R.U., 2024. Removal of per- and polyfluoroalkyl substances by anion exchange resins: scale-up of rapid small-scale column test data. Water Res. 249, 120956.

Cousins, I.T., Johansson, J.H., Salter, M.E., Sha, B., Scheringer, M., 2022. Outside the safe operating space of a new planetary boundary for per- and polyfluoroalkyl substances (PFAS). Environ. Sci. Technol. 56 (16), 11172–11179.

Crittenden, J.C., Berrigan, J.K., Hand, D.W., 1986. Design of rapid small-scale adsorption tests for a constant diffusivity. J. Water Pollut. Control Fed. 58 (4), 312–319.

Crittenden, J.C., Berrigan, J.K., Hand, D.W., Lykins, B., 1987. Design of rapid fixed-bed adsorption tests for nonconstant diffusivities. J. Environ. Eng. 113 (2), 243–259.

Crone, B.C., Speth, T.F., Wahman, D.G., Smith, S.J., Abulikemu, G., Kleiner, E.J., Pressman, J.G., 2019. Occurrence of per- and polyfluoroalkyl substances (PFAS) in source water and their treatment in drinking water. Crit. Rev. Environ. Sci. Technol. 49 (24), 2359–2396.

Cui, J., Zhu, W., Gao, N., Li, J., Yang, H., Jiang, Y., Seidel, P., Ravoo, B.J., Li, G., 2014. Inverse opal spheres based on polyionic liquids as functional microspheres with tunable optical properties and molecular recognition capabilities. Angew. Chem. Int. Ed. 53 (15), 3844–3848.

Danish Ministry of Environment and Gender Equality (Miljøministeriet), 2021. The drinking water ordinance (Bekendtgørelse Om Vandkvalitet Og Tilsyn Med Vandforsyningsanlæg): BEK nr 2361 af 26/11/2021. Danish Ministry of Environment and Gender Equality (Miljøministeriet) (accessed 18.02.2026). https://www.retsinformation.dk/eli/lta/2021/2361.

Das, S., Ronen, A., 2022. A review on removal and destruction of per- and polyfluoroalkyl substances (PFAS) by novel membranes. Membranes 12 (7), 662.

Dixit, F., Dutta, R., Barbeau, B., Berube, P., Mohseni, M., 2021. PFAS removal by ion exchange resins: a review. Chemosphere 272, 129777.

Dong, Z., Ji, G., Wang, F., Wang, F., 2025. Per- and polyfluoroalkyl substances (PFAS): current prevalence, regulatory frameworks, and safe drinking water guidelines in the United States. J. Environ. Chem. Eng. 13 (5), 118145.

Drinking Water Inspectorate, 2025. Guidance on the Water Supply (Water Quality) Regulations 2016 (as amended) for England and Water Supply (Water Quality) Regulations 2018 for Wales specific to PFAS (per- and polyfluoroalkyl substances) in drinking water: guidance to water companies. Drinking Water Inspectorate (accessed 18.02.2026). https://dwi-production-files.s3.eu-west-2.amazonaws.com/wp-content/uploads/2025/03/24141825/DWI_PFAS-Guidance_Mar_2025.pdf.

Du, Z., Deng, S., Zhang, S., Wang, B., Huang, J., Wang, Y., Yu, G., Xing, B., 2016. Selective and high sorption of perfluorooctanesulfonate and perfluorooctanoate by fluorinated alkyl chain modified montmorillonite. J. Phys. Chem. C 120 (30), 16782–16790.

Ellis, A.C., Boyer, T.H., Strathmann, T.J., 2025. Regeneration of conventional and emerging PFAS-selective anion exchange resins used to treat PFAS-contaminated waters. Sep. Purif. Technol. 355, 129789.

European Parliament, 2020. Drinking Water Directive: 2020/2184. European Parliament (accessed 18.02.2026). https://eur-lex.europa.eu/eli/dir/2020/2184.

Federal Republic of Germany (Bundesrepublik Deutschland), 2023. Drinking Water Ordinance (Trinkwasserverordnung): Bgbl I Nr 159. Federal Republic of Germany (Bundesrepublik Deutschland) (accessed 18.02.2026). https://www.recht.bund.de/bgbl/1/2023/159/regelungstext.pdf?_blob=publicationFile&v=2.

Freilinger, J., Back, J.O., Plangger, R., Schottenberger, H., Huck, C.W., Rupprich, M., Bakry, R., 2025a. Development of a fluorophilic ion-exchange material with dual binding mechanism for solid-phase extraction of PFAS. J. Hazard. Mater. Lett. 6, 100158.

Freilinger, J., Gelbrich, T., Braun, D.E., Griesser, U.J., Bakry, R., Kahlenberg, V., Müller, T., Kreutz, C., Nerdinger, S., Fliri, L., Schottenberger, H., 2025b. Ammonium 6:2 fluorotelomer sulfonate: crystal structure, thermal analysis and use as internal standard in PFAS analysis. J. Mol. Struct. 1327, 141232.

Fu, K., Huang, J., Luo, F., Fang, Z., Yu, D., Zhang, X., Wang, D., Xing, M., Luo, J., 2024. Understanding the selective removal of perfluoroalkyl and polyfluoroalkyl substances via fluorine-fluorine interactions: a critical review. Environ. Sci. Technol.

Gagliano, E., Sgroi, M., Falciglia, P.P., Vagliasindi, F.G.A., Roccaro, P., 2020. Removal of poly-and perfluoroalkyl substances (PFAS) from water by adsorption: role of PFAS chain length, effect of organic matter and challenges in adsorbent. Water Res. 171, 115381.

Gelbrich, T., Freilinger, J., Partl, G.J., Schottenberger, H., Kahlenberg, V., Back, J., Nerdinger, S., 2026. Crystal structure of [1046127-79-0], 3,3′-(n-Hexane-1,6-diyl)bis (1-vinylimidazolium) bromide. Molbank 2026 (1), M2138.

Glüge, J., Scheringer, M., Cousins, I.T., DeWitt, J.C., Goldenman, G., Herzke, D., Lohmann, R., Ng, C.A., Trier, X., Wang, Z., 2020. An overview of the uses of per- and polyfluoroalkyl substances (PFAS). Environ. Sci. Process. Impacts 22 (12), 2345–2373.

Gurau, G., Rodríguez, H., Kelley, S.P., Janiczek, P., Kalb, R.S., Rogers, R.D., 2011. Demonstration of chemisorption of carbon dioxide in 1,3-dialkylimidazolium acetate ionic liquids. Angew. Chem. Int. Ed. 50 (50), 12024–12026.

He, C., Yang, Y., Hou, Y.-J., Luan, T., Deng, J., 2022. Chitosan-coated fluoro-functionalized covalent organic framework as adsorbent for efficient removal of per- and polyfluoroalkyl substances from water. Sep. Purif. Technol. 294, 121195.

He, Y., Cheng, X., Gunjal, S.J., Zhang, C., 2024. Advancing PFAS Sorbent design: mechanisms, challenges, and perspectives. ACS Mater. Au. 4 (2), 108–114.

Hollóczki, O., Terleczky, P., Szieberth, D., Mourgas, G., Gudat, D., Nyulászi, L., 2011. Hydrolysis of imidazole-2-ylidenes. J. Am. Chem. Soc. 133 (4), 780–789.

Houtz, E.F., Higgins, C.P., Field, J.A., Sedlak, D.L., 2013. Persistence of perfluoroalkyl acid precursors in AFFF-impacted groundwater and soil. Environ. Sci. Technol. 47 (15), 8187–8195.

Huang, J., Fu, K., Liu, H., Zhang, J., Luo, J., 2025. Unveiling the differential intensity of fluorous active sites toward selective polyfluoroalkyl substance removal: insights into adsorption and desorption trade-offs. Environ. Sci. Technol. 59 (21), 10650–10661.

Huang, P.-J., Hwangbo, M., Chen, Z., Liu, Y., Kameoka, J., Chu, K.-H., 2018. Reusable functionalized hydrogel sorbents for removing long- and short-chain perfluoroalkyl acids (PFAAs) and GenX from aqueous solution. ACS Omega 3 (12), 17447–17455.

Ilić, N., Tan, K., Mayr, F., Hou, S., Aumeier, B.M., Morales, E.M.C., Hübner, U., Cookman, J., Schneemann, A., Gagliardi, A., Drewes, J.E., Fischer, R.A., Mukherjee, S., 2025. Trace adsorptive removal of PFAS from water by optimizing the UiO-66 MOF interface. Adv. Mater. 37 (6), e2413120.

Koda, Y., Terashima, T., Takenaka, M., Sawamoto, M., 2015. Star polymer gels with fluorinated microgels via Star-Star coupling and cross-linking for water purification. ACS Macro Lett. 4 (4), 377–380.

Kumarasamy, E., Manning, I.M., Collins, L.B., Coronell, O., Leibfarth, F.A., 2020. Ionic fluorogels for remediation of per- and polyfluorinated alkyl substances from water. ACS Cent. Sci. 6 (4), 487–492.

Lai, J., Gladden-Bennett, E.F., Shimizu, K., Elstone, N.S., Tanner, T.F.N., Demé, B., Whitwood, A.C., Shimizu, S., Canongia Lopes, J.N., Slattery, J.M., Bruce, D.W., 2025. To mix or not to mix: charge and polarity effects on alkyl/fluoroalkyl compound miscibility. Phys. Chem. Chem. Phys. 27 (26), 13870–13883.

Li, C., Zhang, C., Gibbes, B., Wang, T., Lockington, D., 2022. Coupling effects of tide and salting-out on perfluorooctane sulfonate (PFOS) transport and adsorption in a coastal aquifer. Adv. Water Resour. 166, 104240.

Li, F., Duan, J., Tian, S., Ji, H., Zhu, Y., Wei, Z., Zhao, D., 2020. Short-chain per- and polyfluoroalkyl substances in aquatic systems: occurrence, impacts and treatment. Chem. Eng. J. 380, 122506.

Lin, E.Z., Nason, S.L., Zhong, A., Fortner, J., Godri Pollitt, K.J., 2023. Trace analysis of per- and polyfluorinated alkyl substances (PFAS) in dried blood spots - demonstration of reproducibility and comparability to venous blood samples. Sci. Total Environ. 883, 163530.

Loos, R., Carvalho, R., António, D.C., Comero, S., Locoro, G., Tavazzi, S., Paracchini, B., Ghiani, M., Lettieri, T., Blaha, L., Jarosova, B., Voorspoels, S., Servaes, K., Haglund, P., Fick, J., Lindberg, R.H., Schwesig, D., Gawlik, B.M., 2013. EU-wide monitoring survey on emerging polar organic contaminants in wastewater treatment plant effluents. Water Res. 47 (17), 6475–6487.

Manning, I.M., Guan Pin Chew, N., Macdonald, H.P., Miller, K.E., Strynar, M.J., Coronell, O., Leibfarth, F.A., 2022. Hydrolytically stable ionic fluorogels for high-performance remediation of per- and polyfluoroalkyl substances (PFAS) from natural water. Angew. Chem. 134 (41).

McCleaf, P., Englund, S., Östlund, A., Lindegren, K., Wiberg, K., Ahrens, L., 2017. Removal efficiency of multiple poly- and perfluoroalkyl substances (PFASs) in drinking water using granular activated carbon (GAC) and anion exchange (AE) column tests. Water Res. 120, 77–87.

Medha, S., Romisher, Z., van Bramer, S., Weyrich, J., Khan, S., Saha, D., 2024. Enhanced adsorption of perfluorooctanesulfonic acid (PFOS) in fluorine doped mesoporous carbon: experiment and simulation. Carbon 218, 118745.

Min, X., Huo, J., Dong, Q., Xu, S., Wang, Y., 2022. Enhanced sorption of perfluorooctanoic acid with organically functionalized layered double hydroxide. Chem. Eng. J. 446, 137019.

Pannu, M.W., Chang, J., Medina, R., Grieco, S.A., Hwang, M., Plumlee, M.H., 2023. Comparing PFAS removal across multiple groundwaters for eight GACs and alternative adsorbent. AWWA Water Sci. 5 (3).

Pannu, M.W., Huang, A., Plumlee, M.H., 2024. Variable PFAS removal by adsorbent media with sufficient prediction of breakthrough despite reduced contact time at pilot scale. Water Environ. Res. 96 (5), e11035.

Partl, G.J., Naier, B.F.E., Bakry, R., Schlapp-Hackl, I., Kopacka, H., Wurst, K., Gelbrich, T., Fliri, L., Schottenberger, H., 2021. Can't touch this: highly omniphobic

coatings based on self-textured C6-fluoroponytailed polyvinylimidazolium monoliths. J. Fluor. Chem. 249, 109839.
Pezoulas, E.R., Tajdini, B., Ko, Y., Uliana, A.A., Giovine, R., Furukawa, H., Vatankhah, H., Börgel, J., Kim, K.C., Bellona, C., Long, J.R., 2025. Functionalized porous polymer networks as high-performance PFAS adsorbents. J. Am. Chem. Soc. 147 (25), 21832–21843.
Quan, Q., Wen, H., Han, S., Wang, Z., Shao, Z., Chen, M., 2020. Fluorous-core nanoparticle-embedded hydrogel synthesized via tandem photo-controlled radical polymerization: facilitating the separation of perfluorinated alkyl substances from water. ACS Appl. Mater. Interfaces 12 (21), 24319–24327.
Riegel, M., Haist-Gulde, B., Sacher, F., 2023. Sorptive removal of short-chain perfluoroalkyl substances (PFAS) during drinking water treatment using activated carbon and anion exchanger. Environ. Sci. Eur. 35 (1).
Roberts, J., McNaughtan, M., de las Heras Prieto, H., 2023. Unwanted ingredients—highly specific and sensitive method for the extraction and quantification of PFAS in everyday foods. Food Anal. Methods 16 (5), 857–866.
Román Santiago, A., Yin, S., Elbert, J., Lee, J., Shukla, D., Su, X., 2023. Imparting selective fluorophilic interactions in redox copolymers for the electrochemically mediated capture of short-chain perfluoroalkyl substances. J. Am. Chem. Soc. 145 (17), 9508–9519.
Ruthven, D.M., 1984. Principles of Adsorption and Adsorption processes. A Wiley-Interscience Publication. Wiley, New York.
Salahudeen, S., Thiel, T.A., Mejía, E., 2024. Chemical degradation of oxygenated polymers: the case of polyethers and polysiloxanes. RSC Sustain. 2 (7), 1904–1929.
Schrenk, D., Bignami, M., Bodin, L., Chipman, J.K., Del Mazo, J., Grasl-Kraupp, B., Hogstrand, C., Hoogenboom, L.R., Leblanc, J.-C., Nebbia, C.S., Nielsen, E., Ntzani, E., Petersen, A., Sand, S., Vleminckx, C., Wallace, H., Barregård, L., Ceccatelli, S., Cravedi, J.-P., Halldorsson, T.I., Haug, L.S., Johansson, N., Knutsen, H. K., Rose, M., Roudot, A.-C., van Loveren, H., Vollmer, G., Mackay, K., Riolo, F., Schwerdtle, T., 2020. Risk to human health related to the presence of perfluoroalkyl substances in food. EFSA J. 18 (9), e06223.
Silva, R.R.A., Marques, C.S., Arruda, T.R., Teixeira, S.C., de Oliveira, T.V., 2023. Biodegradation of polymers: stages, measurement, standards and prospects. Macromol 3 (2), 371–399.
Singh, A., Lynch, R., Solomon, J., Weaver, J.D., May, A.R., 2023. Development of novel fluor mop materials for remediation of perfluoroalkyl substances (PFAS) from groundwater. J. Hazard. Mater. 448, 130853.
Sun, Y., Patyal, A.S., Hana, G., Wu, K., Real, I., Zhou, C., Guelfo, J.L., Howe, J.D., Shen, Y., 2026. Adsorption of per- and polyfluoroalkyl substances (PFAS) by quaternary ammonium and fluorine-functionalized macrocyclic sorbents: a comprehensive experimental and simulation study. Water Res. 290, 125006.
Swedish Food Agency (Livsmedelsverket), 2023. PFAS and other environmental toxins in drinking water and food - control (Riskhantering PFAS i dricksvatten och egenfångad fisk). Swedish Food Agency (Livsmedelsverket) (accessed 18.02.2026). https://www.livsmedelsverket.se/foretagande-regler-kontroll/dricksvattenproduktion/kontroll-pfas-miljogifter-dricksvatten-egenfangad-fisk/.
Tan, X., Dewapriya, P., Prasad, P., Chang, Y., Huang, X., Wang, Y., Gong, X., Hopkins, T. E., Fu, C., Thomas, K.V., Peng, H., Whittaker, A.K., Zhang, C., 2022a. Efficient removal of perfluorinated chemicals from contaminated water sources using magnetic fluorinated polymer sorbents. Angew. Chem. Int. Ed. 61 (49), e202213071.
Tan, X., Sawczyk, M., Chang, Y., Wang, Y., Usman, A., Fu, C., Král, P., Peng, H., Zhang, C., Whittaker, A.K., 2022b. Revealing the molecular-level interactions between cationic fluorinated polymer sorbents and the major PFAS pollutant PFOA. Macromolecules 55 (3), 1077–1087.
Tan, X., Zhong, J., Fu, C., Dang, H., Han, Y., Král, P., Guo, J., Yuan, Z., Peng, H., Zhang, C., Whittaker, A.K., 2021. Amphiphilic perfluoropolyether copolymers for the effective removal of polyfluoroalkyl substances from aqueous environments. Macromolecules 54 (7), 3447–3457.
Wadsö, L., Karlsson, O.J., 2013. Alkaline hydrolysis of polymers with ester groups studied by isothermal calorimetry. Polym. Degrad. Stab. 98 (1), 73–78.
Wang, W., Xu, Z., Zhang, X., Wimmer, A., Shi, E., Qin, Y., Zhao, X., Zhou, B., Li, L., 2018. Rapid and efficient removal of organic micropollutants from environmental water using a magnetic nanoparticles-attached fluorographene-based sorbent. Chem. Eng. J. 343, 61–68.
Xiao, L., Ling, Y., Alsbaiee, A., Li, C., Helbling, D.E., Dichtel, W.R., 2017. β-cyclodextrin polymer network sequesters perfluorooctanoic acid at environmentally relevant concentrations. J. Am. Chem. Soc. 139 (23), 7689–7692.
Xie, R., Zhou, L., Smith, A.E., Almquist, C.B., Berberich, J.A., Danielson, N.D., 2022. A dual grafted fluorinated hydrocarbon amine weak anion exchange resin polymer for adsorption of perfluorooctanoic acid from water. J. Hazard. Mater. 431, 128521.
Yang, A., Ching, C., Easler, M., Helbling, D.E., Dichtel, W.R., 2020. Cyclodextrin polymers with nitrogen-containing tripodal crosslinkers for efficient PFAS adsorption. ACS Mater. Lett. 2 (9), 1240–1245.
Ye, X., Zuo, B., Deng, M., Hei, Y., Ni, H., Lu, X., Wang, X., 2010. Surface segregation of fluorinated moieties on poly(methyl methacrylate-ran-2-perfluorooctylethyl methacrylate) films during film formation: entropic or enthalpic influences. J. Colloid Interface Sci. 349 (1), 205–214.
Zhang, D.Q., Zhang, W.L., Liang, Y.N., 2019. Adsorption of perfluoroalkyl and polyfluoroalkyl substances (PFASs) from aqueous solution - a review. Sci. Total Environ. 694, 133606.